Three-dimensional flow and load characteristics of flexible revolving wings at low Reynolds number

van de Meerendonk, Remco; Perçin, Mustafa; van Oudheusden, Bas

Publication date
2016

Document Version
Accepted author manuscript

Published in
Proceeedings of the 18th International Symposium on the Application of Laser and Imaging Techniques to Fluid Mechanics

Three-dimensional flow and load characteristics of flexible revolving wings at low Reynolds number

Remco van de Meerendonk[1*], Mustafa Percin[1], Bas van Oudheusden[1]
1: Dept. of Aerospace Engineering, Delft University of Technology, the Netherlands
* Correspondent author: remcovandemeerendonk@gmail.com

Keywords: Flapping wing, Force/ Pressure from PIV data, Unsteady aerodynamics, Vortex flows

ABSTRACT

This study explores the flow field and fluid-dynamic loads generated by revolving low-aspect-ratio flat plate wings undergoing a revolving motion starting from rest. Three wings with different degree of chordwise flexural stiffness (i.e., rigid, moderate flexibility and high flexibility) have been tested in order to investigate the influence of the wing flexibility. The wings have an angle of attack of 45 deg in their undeformed condition. The measurements have been performed in a water tank at a Reynolds number of 10,000 based on the chord length and terminal velocity at the 75% span position. The experimental campaign consists of phase-locked tomographic particle image velocimetry measurements complemented with simultaneous force measurements The three-dimensional velocity fields are captured in three measurement volumes positioned side-by-side along the span of the wing for different phases of the revolving motion, generating a time-resolved volumetric velocity field data set. Subsequently, from the velocity data the pressure fields are reconstructed as well as the loads acting on the wing.

The force measurements reveal that the lift generation of the rigid and moderately flexible wings is comparable while it is slightly reduced for the highly flexible wing. The drag shows a monotonic decrease with decreasing flexural stiffness. Consequently the lift-to-drag ratio is increased significantly with decreasing flexural stiffness and is found to correlate well with the geometric angle of attack of the deformed wing. The PIV measurements reveal a vortex system consisting of a leading edge vortex (LEV), a trailing edge vortex (TEV), a tip vortex (TV) and a root vortex (RV) that forms at the onset of the motion. For decreasing flexural stiffness, the coherency of this vortex system and spanwise transport of vorticity in the LEV is increased, which contributes to the stability and retention of the LEV. The vortex system structures encompass a low pressure region which has a high correlation with the vortical structures. As the low pressure region accompanying the LEV becomes smaller with increasing flexibility, the total force acting on the wing is reduced, but it is also tilted more towards the lift direction due to the wing deformation. As a consequence, the lift component remains relatively high, also because the suction peak is located closer to the wing surface. Simultaneously, the drag is significantly suppressed for increasing flexibility, which is also reflected in the smaller size of the wake. While the sectional lift along the full span is comparable for the different wings, the sectional drag is significantly reduced at the outboard wing locations for increasing flexibility.

1. Introduction

Increasing interest in the field of micro air vehicles (MAVs) has stimulated research activities regarding biological flapping-wing flight since other means of force generation (i.e., fixed-wing and rotary-wing mechanisms) suffer from deteriorated aerodynamic performance at the flight regime of MAVs which is characterized by low Reynolds numbers. Flapping-wing flight is characterized by unsteady three-dimensional effects, where the formation of a stable leading edge vortex (LEV) is one of the most prominent mechanisms responsible for the enhanced aerodynamic forces sustaining flapping flight (Sane, 2003). The LEV phenomenon in the context of flapping-wing aerodynamics has been subject to a number of studies in the last three decades, particularly to achieve a better understanding of its formation and the mechanisms responsible for its stability. It has been hypothesized that spanwise pressure gradients and the associated vorticity transport (Ellington et al. 1996) and the apparent rotational accelerations which are characterized by the Rossby number (Lentink & Dickinson 2009, Jardin and David 2014, 2015) play an important role in this respect.

The sweeping (translational) aspect of the full flapping-wing motion can be represented by a revolving wing model, in which these rotational inertial mechanisms and spanwise gradients are also present. Accordingly, the flow fields and force generation aspects of revolving low-aspect-ratio wings have been studied for a wide range of parameters as reported in the literature. Jones & Babinsky (2011) considered a rectangular revolving flat-plate wing with an aspect ratio of 4. The force levels and flow structures were not observed to change significantly over the range of Reynolds numbers investigated (10,000 to 60,000). Ozen & Rockwell (2012) investigated a similar revolving rectangular wing with an aspect ratio of 1 and a Rossby number of $R_o/c = 1.02$ for a range of Reynolds numbers from 3,600 to 14,500 at different angles of attack. A stable LEV was observed for angles of attack between 30 deg and 75 deg. Recently, Percin & van Oudheusden (2015a) studied a rectangular flat-plate wing of aspect ratio 2 and a Rossby number of $R_o/c = 1.8$, undergoing a revolving-surging motion accelerating from rest. In the Reynolds number range of 5,000 to 25,000 the force and vorticity generation was found to increase with the Reynolds number. For a range of angles of attack from 15 deg to 75 deg, the behavior of the vortical structures was found to be similar, however their morphology is altered by the promoted separation at higher angles of attack.

An important characteristic of biological flapping-wing flight that is not commonly taken into account in mechanical model simulations like those referred to above, is the influence of wing flexibility. Different studies have indicated the possible benefits of flexibility on the aerodynamic performance (Shyy et al., 2010). Combes & Daniel (2003) found that for biological flyers the wing size is the dominant factor in flexural stiffness scaling and that the spanwise flexural stiffness is 1-2 orders of magnitude higher than the chordwise flexural stiffness. Zhao et al. (2009) studied wings with different chordwise stiffness for different angles of attack at a Reynolds number of 2,000 for a steady revolving motion. It was observed that the lift-to-drag ratio is relatively insensitive to wing flexibility for angles of attack from 20 deg to 60 deg, while the ability to generate both lift and drag decreased. Zhao et al. (2011) found that flexibility does not fundamentally change the aerodynamic flow structures, but that the LEV is smaller for lower flexural stiffness (higher flexibility) and correlates with the aerodynamic forces. Beals & Jones (2015) studied a passive chordwise-flexible revolving wing for Reynolds numbers from 10,000 to 25,000. For the flexible wing the lift was measured to be consistently lower than that of the rigid wing throughout the revolving motion, however, passive wing deformation mitigated the lift losses when a wake was encountered, i.e. for rotation angles larger than 360 degrees.

So far, the study of revolving flexible wings has been largely based on force measurement and qualitative (dye) visualization. Further quantitative information regarding the flow field development and its connection to the force generation will be instrumental in improving the understanding of the effect of wing flexibility on the aerodynamic performance of revolving wings. Recent advancements in volumetric imaging capabilities, notably tomographic particle image velocimetry (PIV) (Elsinga et al., 2006; Scarano, 2013) have motivated the current experimental investigation to further investigate the effects of wing flexibility in the context of flapping wing aerodynamics in more detail. Experimental studies focusing on the volumetric measurements of flow fields around flapping wings are scarce. Percin & van Oudheusden (2015b) acquired three-component three-dimensional (3D3C) flow fields around revolving-surging and revolving-pitching rigid flat-plate wings for an angle of attack of 45° and a Reynolds number of 10,000 by means of tomographic PIV. A detailed analysis of the enhanced forces of the revolving-pitching motion was given. Carr et al. (2013) studied a rigid rectangular revolving flat-plate wing for an angle of attack of 45 deg and a Reynolds number of 5,000 using phase-locked and phase-averaged stereoscopic PIV for different chord planes to reconstruct phase-averaged spanwise 3D3C velocity data sets. Detailed analysis was made for wings of aspect ratio 2 and 4. For an aspect ratio of 2 the overall LEV- tip vortex (TV) structure remains more coherent and is

located closer to the wing surface. The vortical structure breaks down after a longer travel distance compared to the wing with an aspect ratio of 4. Wolfinger & Rockwell (2014) studied a rigid rectangular revolving flat-plate wing at an angle of attack of 45 deg and a Reynolds number of 1,400 for different Rossby numbers using a similar experimental setup. An increased coherency of the vortex system was observed for lower Rossby numbers and it was suggested that the stability or retention of the LEV is coupled with the interior structure of the tip and root vortices.

The sustained LEV occurring in a revolving motion is accompanied by a low pressure region at the suction side of the airfoil. The suction forces that act normal to the wing surface are dominant such that for a rigid wing the resultant force vector acts normal to the wing chord for angles of attack higher than 10 deg (Usherwood & Ellington, 2002; Birch, 2004). Therefore, the link between the temporal evolution of the vortical structures and the associated pressure forces can be obtained properly when incorporating the pressure field in the analysis. In this respect, Tronchin et al. (2015) experimentally studied the loads and pressure field for a flapping wing at a Reynolds number of 1,000 using 3D3C velocity data obtained from phase-averaged cross-correlated stereo-PIV planes. The acceleration information is determined in an inertial frame by acquiring, per phase angle, 5 volumetric images with small time shifts and subsequently calculating the acceleration from the velocity fields furthest separated in time, with a corresponding temporal resolution of 150 ms. This study suggests that the calculated pressure field is obtained with sufficient accuracy for a global analysis of the topology of the flow field and the evaluation of loads acting on an immersed object.

The aim of the current study is to investigate the spatial-temporal evolution of the flow field of revolving low-aspect-ratio wings, and to connect the associated vortical structures and pressure fields to the temporal evolution of the fluid-dynamic forces acting on the wing. Wings with different degree of chordwise flexibility are considered, to study the influence of wing deformation on the aerodynamics of the wings. For this purpose, phase-locked tomographic PIV measurements were performed in three volumes along the wing span for different phases of the revolving motion in order to obtain time-resolved 3D3C flow field data sets around the wing. Simultaneous force measurements were carried out by means of a six-component water submergible force sensor to obtain the temporal variation of the forces during the revolving motion. Pressure fields are reconstructed from the PIV data, which also enables the calculation of forces acting on the wing from the flow fields by use of a control-volume approach.

2. Experimental Methods

Experimental Setup & Model description

The experiments were conducted in a water tank (Fig. 1) at the Aerodynamics Laboratory of Delft University of Technology (TU Delft). The octagonal tank (600 mm in diameter and 600 mm in height) is made of Plexiglas walls allowing full optical access for illumination and imaging (Fig. 1). The main axis of the driving system is mounted vertically in the water tank. The revolving motion of the model is controlled by a brushed DC motor and a gearbox (gear ratio of 132:1). A submerged servo motor connected to the wing is used to control the angle of attack, which is set to 45 deg in the present experiments. The model consists of a flat plate with a chord length (c) of 50 mm and a wing span length (R) of 100 mm, resulting in a wing aspect ratio of 2. At the leading edge a 1.5 mm radius halfround carbon fiber rod is glued on the upper and lower side of the wing to provide spanwise rigidity. This leading edge structure is clamped in the mount with a 1 mm offset from the wing root. The distance between the root and the rotation axis is 42 mm giving a radius of gyration of $R_g = 96.4$ mm and a corresponding Rossby number of approximately $R_g/c = 1.93$.

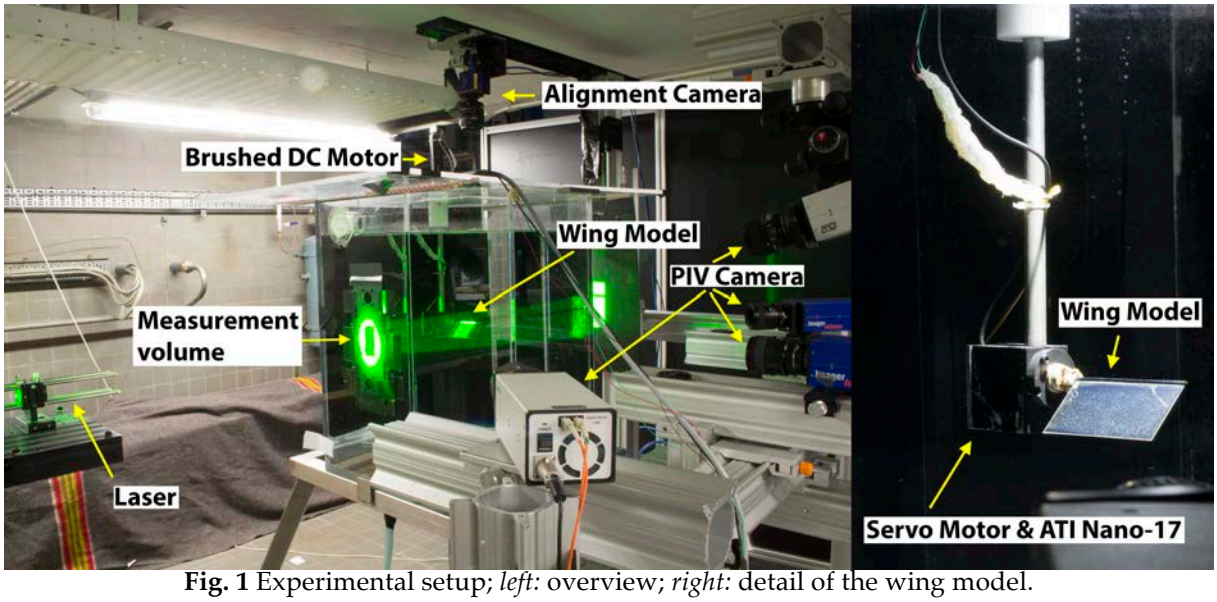

Fig. 1 Experimental setup; *left:* overview; *right:* detail of the wing model.

Kinematics & Flexibility

The 75% span position of the wing model is taken as the reference position to characterize the motion kinematics. The non-dimensional parameters describing the motion kinematics are: convective time ($t^* = t \cdot V_t/c$, where t is time in seconds and V_t is the constant terminal velocity established after the acceleration phase) and chords travelled ($\delta^* = \delta/c$, where δ is the distance travelled by the wing at the reference spanwise position). The revolving wing motion starts from rest and is subjected to a constant acceleration to reach a pre-defined V_t of 0.2 m/s over a time interval corresponding to a displacement of one chord length (i.e. $0 < \delta^* < 1$), after which the wing continues to revolve at a constant velocity (i.e. for $\delta^* > 1$). Based on the chord length and the terminal velocity the Reynolds number is 10,000. The chordwise flexural stiffness is approximated by using EI, where E is the Young's modulus and $I = Rh^3/12$ is the area moment of inertia of the wing's cross section along the chord, R and h being the wing span (100 mm) and thickness (variable), respectively. Three models with different flexural stiffness have been studied by changing the material and plate thickness as given in Table 1.

Tab. 1 Model Parameters. (PET properties: Hostaphan GN, Mitsubishi polyester film GmbH.)

Material	Young's modulus E [Nm^{-2}]	Thickness h [mm]	Flexural stiffness EI [Nm^2]	*Description*
Plexiglass	~3300·10^6	1	2.75·10^{-2}	*1 [mm] Rigid*
PET	~4350·10^6	0.175	1.94·10^{-4}	*175 [µm] Moderate flexibility*
	~4500·10^6	0.125	7.32·10^{-5}	*125 [µm] High flexibility*

The PIV measurements were taken for the interval $0.0625 < \delta^* < 4$. For the rigid case the temporal resolution (TR) is set to 62.5 ms for the entire interval, which corresponds to a non-dimensional temporal resolution ($TR^* = TR \cdot V_t/c$) of 0.25, generating 19 revolving phases. For the flexible wings, the $TR^* = 0.25$ for $0.0625 < \delta^* < 1.5$ and $TR^* = 0.5$ for $1.5 < \delta^* < 4$, generating a total of 14 revolving phases. The three-dimensional flow fields were ensemble averaged with a sample size of 5 obtained by repeating the measurements for each phase. The force measurements are performed for an extended time interval of $0 < \delta^* < 14$. The prescribed wing kinematics for the phase angles of the PIV measurements is illustrated in Fig. 2.

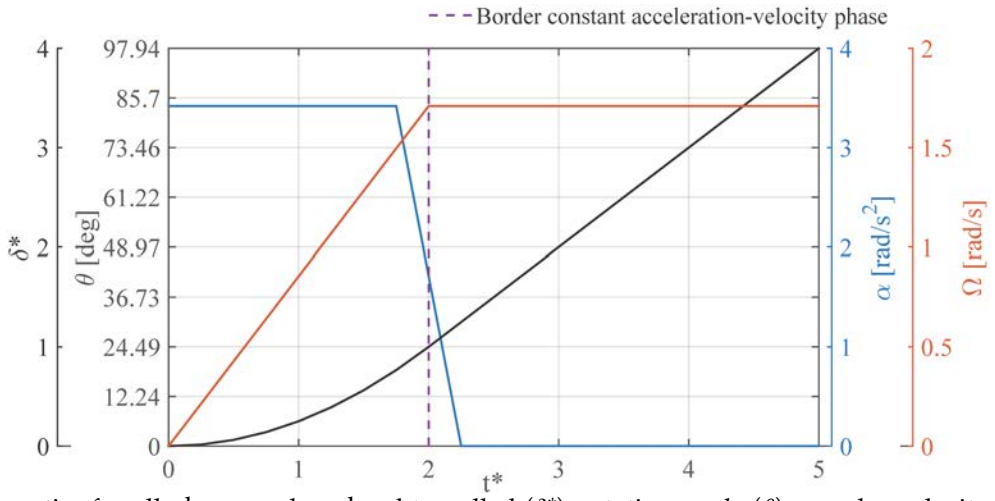

Fig. 2 Wing kinematics for all phase angles: chord travelled (δ^*), rotation angle (θ), angular velocity (Ω) and angular acceleration (α) as a function of convective time (t^*).

Force measurements

The forces and moments exerted on the wings were measured with a water-submergible ATI Nano17/IP68 force sensor. The sensor is calibrated to have a maximum sensing value of 25 N in x, y and 35 N in z-direction with a resolution of 1/160 N, and a torque capacity of 250 N·mm with a resolution 1/32 N·mm. The force and moment data were acquired at 2 kHz acquisition frequency via a LabVIEW code, which also controls the motors and synchronizes the wing motion with the force data acquisition and the PIV measurements. For ensemble averaging of the force signals, about 260 data records were used for the rigid wing and 200 for the flexible wings. From the 3 wing models, the test-rig for the rigid wing was observed to have the lowest natural frequency, which is 10 Hz. To eliminate electronic noise, effects of mechanical vibrations from the driving system and resonance of the test-rig, the ensemble averaged force data is filtered with a Chebyshev II low-pass filter that has a cut-off frequency of 8 Hz with a stopband attenuation of 80 dB. A forward-backward filtering technique is applied to prevent a time-shift of the data. Lift and drag coefficients are defined with respect to the reference velocity, which is the terminal wing velocity at the 75% span reference plane.

Volumetric flow imaging by tomographic PIV

Fig. 3-*left* shows a schematic top view of the tomographic PIV setup. Four 12-bit PCO Sensicam CCD cameras were used to record the particle images. Camera 1, 3 and 4 have a resolution of 1376×1040 pixels and a pixel pitch of 6.45 μm and are arranged on the same horizontal x-z plane with an aperture angle of 90 deg. Camera 2 has a resolution of 1280×1024 pixels and a pixel pitch of 6.7 μm and is located above camera 3 with an aperture angle of 20 deg with respect to the horizontal plane. Double-frame images are taken at the moment in the motion when the wing is oriented normal to camera 3 and data for different revolving phases are obtained by

appropriately changing the starting position of the wing revolution. Each camera was equipped with a Nikon 60 mm focal objective at a numerical aperture $f_\# = 16$. Scheimpflug adapters were used on the three off-axis cameras to align the mid-plane of the measurement volume with the focal plane. The volume was illuminated by a double-pulsed Nd:Yag laser at a wavelength of 532 nm. Polyamide spherical particles of 56 μm diameter were used as tracer particles.

The full flow field around the wing is captured by combining three tomographic measurement volumes, each measuring 100×75×45 mm in the x,y,z-directions, respectively, as shown in Fig. 3. The corresponding magnification factor is approximately 0.09. The volumes are symmetric with respect to the mid-span plane of the wing and have an overlap of 5 mm (≈ 6 vectors). The illumination volume was kept at a fixed position in the water tank, which corresponds to measurement volume 2 as indicated in Fig. 3-*left*. To change the measurement volume, the complete driving system including wing was translated along the direction corresponding to the viewing direction of camera 3. The image resolution is approximately 13.76 pixels/mm (≈ 688 pixels/c). The particle images are interrogated using windows with a final size of 48×48×48 voxels with an overlap factor of 75% giving an approximate spatial resolution of 0.87 mm/vector (≈ 57 vectors/c).

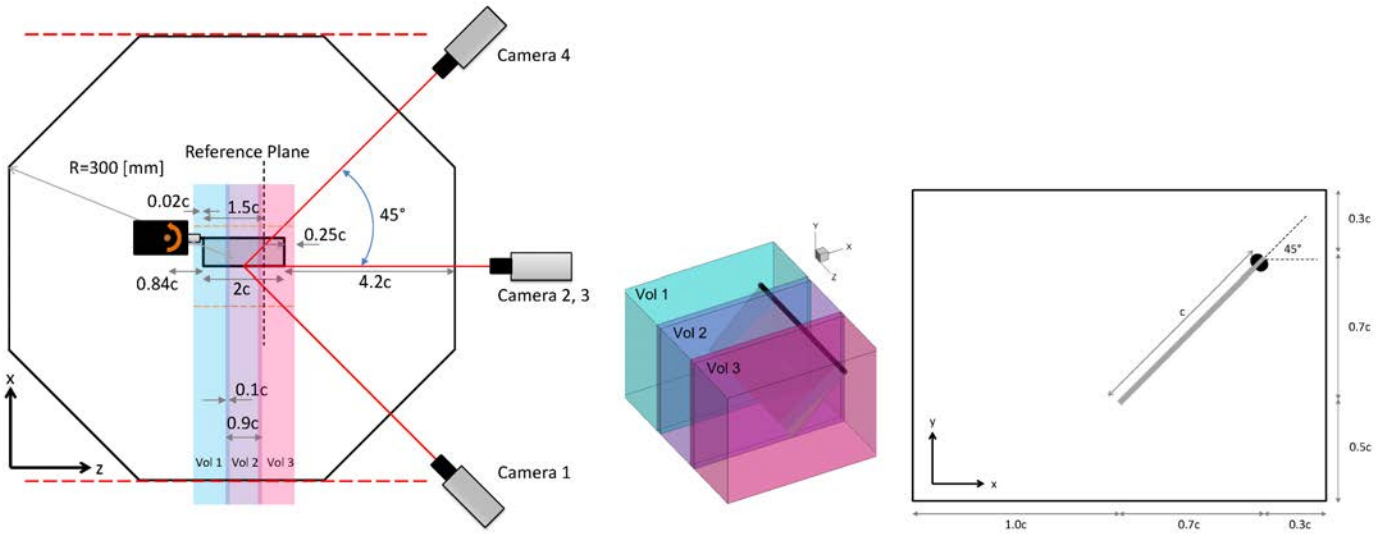

Fig. 3 *Left*: Schematic top view and experimental setup. *Middle*: Schematic of the measurement volumes. *Right*: Schematic representation of the chordwise field of view. Schematics illustrated with a rigid wing.

Wing reconstruction

The wing is reconstructed by use of a number of tracer points along the wing model. By visually identifying these points in all camera images and using the imaging calibration information, these points are reconstructed in 3D space. The chordwise deflection at the tip is reconstructed by defining equidistant points between the leading and trailing edge points in all images and

further triangulation of these points (note that the leading edge point is defined on the wing surface after the carbon fiber rod).

At the leading edge, the angle of attack (AoA) is set to 45 deg by the servo motor at the beginning of the experiment. However, the flexible wings deform during the revolving motion under the effect of hydrodynamic loads which changes the geometric angle of attack. For the deformed flexible wings, the geometric angle of attack for a given spanwise location is defined as the angle between the wing motion and the line connecting the reconstructed leading edge and trailing edge points. Subsequently, the twist angle is obtained by measuring the geometric angle of attack at 4 spanwise positions, after which a second degree polynomial is fitted to represent the spanwise variation of the geometric angle of attack. The average uncertainty in the triangulation of the identified points at the tip is approximately 0.3 of the vector spacing, corresponding to an uncertainty of 0.6 deg in the geometric angle of attack. On the other hand, the variation in the local angle of attack along the chord, which reflects the curvature of the wing, is computed from the gradients between the chordwise reconstructed points. The deflection of the rigid wing is negligible such that it can be assumed to be fully rigid with a fixed geometric and local angle of attack of 45 deg for all phase angles.

3. Data processing

The instantaneous pressure field reconstruction is carried out under the assumption of incompressible flow, employing the Navier-Stokes equations (van Oudheusden, 2013), while the loads are reconstructed using a control volume approach (Anderson, 2011). The experiments are performed in water with a constant density (ρ) of approximately 1,000 kg/m^3 and dynamic viscosity (μ) of approximately $1 \cdot 10^{-3}$ $N \cdot s/m^2$. At low Reynolds numbers the flow is very repeatable for the same kinematic motion, which justifies the use of phase-locked measurements (Poelma et al., 2006; Percin & van Oudheusden, 2015b). In view of this phase-locked measurement procedure, the pressure reconstruction is most conveniently set up in the rotating reference frame aligned with the revolving wing, regarding the evaluation of the temporal derivatives from the phase-locked flow field data sets. In the evaluation of the material derivative the Eulerian approach is expected to be more sensitive to advective motion, while the Lagrangian is more sensitive to rotation-dominated flows because this complicates the flow path reconstruction (de Kat & van Oudheusden, 2012). Within a rotating reference frame the dominance of rotation over advective motion is increased compared to an inertial frame, such that the Eulerian approach

may be anticipated to perform better for evaluating the material derivative. Note that, as the pressure is a scalar quantity, the reconstructed surfaces of constant pressure are independent of the reference frame (inertial or moving) that is used (Vanyo, 2015).

The flow fields obtained in the PIV measurements are defined in the inertial "laboratory" reference frame. The velocity field data is converted from the inertial reference frame to the rotating reference frame as,

$$\mathbf{u}_{\text{rotating}} = \mathbf{u}_{\text{inertial}} - \Omega \times \mathbf{r}_{\text{pv}} \quad (1)$$

where $\mathbf{u}$ is the velocity vector, Ω the angular velocity of the wing and $\mathbf{r}_{\text{pv}}$ the position vector measured from the rotation axis ($0.84c$ offset in z-direction with respect to the root of the wing, as depicted in Fig. 3). In the remainder of this section the considered velocity is the apparent velocity in the rotating reference frame.

Assuming incompressible flow, a constant viscosity and discarding gravity, the pressure gradients in the rotating reference frame are evaluated as,

$$\frac{1}{\rho}\nabla p = -\frac{D\mathbf{u}}{Dt} - \underbrace{\boldsymbol{\Omega}\times(\boldsymbol{\Omega}\times\mathbf{r}_{\text{pv}})}_{\text{Centrifugal}} - \underbrace{2\,\boldsymbol{\Omega}\times\mathbf{u}}_{\text{Coriolis}} - \underbrace{\frac{d\boldsymbol{\Omega}}{dt}\times\mathbf{r}_{\text{pv}}}_{\text{Euler}} + \nu\nabla^2\mathbf{u} \quad (2)$$

where p is the pressure and ν is the kinematic viscosity. The centrifugal, Coriolis and Euler effects introduce apparent forces due to working in a non-inertial reference frame. The material derivative $D\mathbf{u}/Dt$ is calculated according to the Eulerian approach, by separately evaluating the local time-derivative and convective terms. Subsequently the pressure gradient field is integrated by setting up a Poisson problem as,

$$\nabla^2 p = \nabla \cdot (\nabla p) \quad (3)$$

The 3D Poisson problem is discretized using a finite second-order-accurate central-difference scheme resulting into a 7-point stencil. At the boundaries of the integration domain Neumann boundary conditions (spatial gradient of pressure) normal to the boundary are imposed. The Neumann boundary conditions are set up using a second order accurate central difference scheme by introducing ghost points outside of the calculation domain.

Due to the presence of the wing in the measurement region, the reconstructed velocity vectors at its location and in the close vicinity have a relatively high uncertainty and need to be excluded from the pressure reconstruction. Based on the position information obtained from the wing reconstruction, a mask around the wing is created. By means of a mask convergence study, the optimum mask size, defined as the smallest size for which converged lift and drag are obtained, was determined to be 7 vectors, as illustrated in Fig. 4.

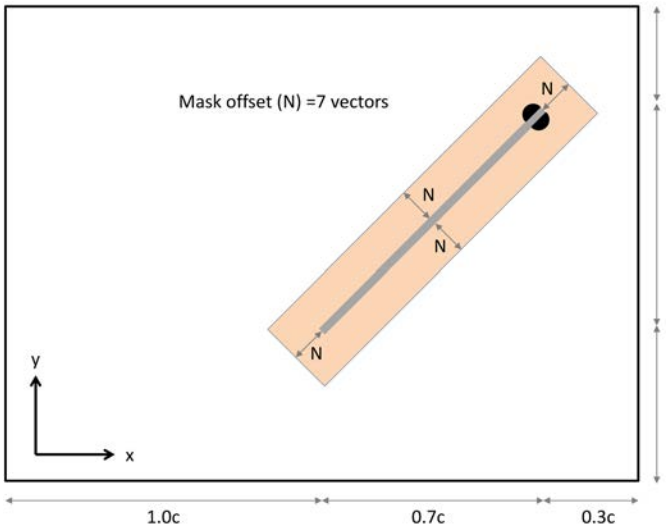

Fig. 4 Mask implementation.

After the pressure fields are obtained for each volume individually, they are scaled with respect to volume 2 at the mid-planes of the overlap regions from volume 1-2 and volume 3-2 (as depicted in Fig. 3) to obtain a smooth transition between volumes. Subsequently, the complete pressure field is expressed with respect to a reference pressure of 0 Pa, that is defined in the lower right corner of the flow field (maximum x-location, minimum y-location) in which the flow is assumed to be undisturbed.

The fluid-dynamic loads are reconstructed by evaluating the integral momentum balance obtained by integrating the Navier-Stokes equation within a control volume. Under the assumption of incompressible flow and in the absence of gravity, the instantaneous force **F** for an impermeable solid object evaluated within a steady control volume is given as,

$$F(t) = -\frac{d}{dt}\rho \int_V \mathbf{u} dV - \rho \int_S \mathbf{u}(\mathbf{u}\cdot\mathbf{n}) dS + \int_S (-p\mathbf{n} + \tau\cdot\mathbf{n}) dS \\ -\rho \int_V \boldsymbol{\Omega}\times(\boldsymbol{\Omega}\times\mathbf{r}_{\mathrm{pv}}) dV - \rho \int_V 2\ \boldsymbol{\Omega}\times\mathbf{u} dV - \rho \int_V \frac{d\boldsymbol{\Omega}}{dt}\times\mathbf{r}_{\mathrm{pv}}\ dV \quad (4)$$

where the control volume V matches the field of view and with is bounded by an external contour S. $\boldsymbol{n}$ is the outward normal on the outer contours and τ is the shear stress. The spatial and temporal derivatives are calculated with a second-order-accurate central-difference scheme, except at the boundaries of the temporal evolution at which a first-order-accurate difference scheme is employed. By evaluating the loads in a thin sectional control volume with dimensions matching the field of view in the x,y-directions and a spanwise thickness of dz in the z-direction

that is centered at a given spanwise plane, the sectional lift & drag coefficient for that spanwise plane can be approximated as,

$$C_l = \frac{L'/dz}{\frac{1}{2}\rho V_t^2 c} = \frac{l}{\frac{1}{2}\rho V_t^2 c} \quad (5) \quad ; \quad C_d = \frac{D'/dz}{\frac{1}{2}\rho V_t^2 c} = \frac{d}{\frac{1}{2}\rho V_t^2 c} \quad (6)$$

where L' and D' are the lift and drag calculated from the sectional control volume.

4. Results

Wing reconstruction

The temporal evolution of the tip deflection and the geometric angle of attack for the flexible wings are given in Fig. 5. Both flexible wings deflect significantly at the tip during the revolving motion. Due to the deflection of the wing the geometric angle of attack decreases as the motion progresses. At $\delta^* = 4$ the approximate geometric angle at the root and tip are respectively 41 deg and 39 deg for the moderate flexible wing, and 34.5 deg and 31 deg for the high flexible wing.

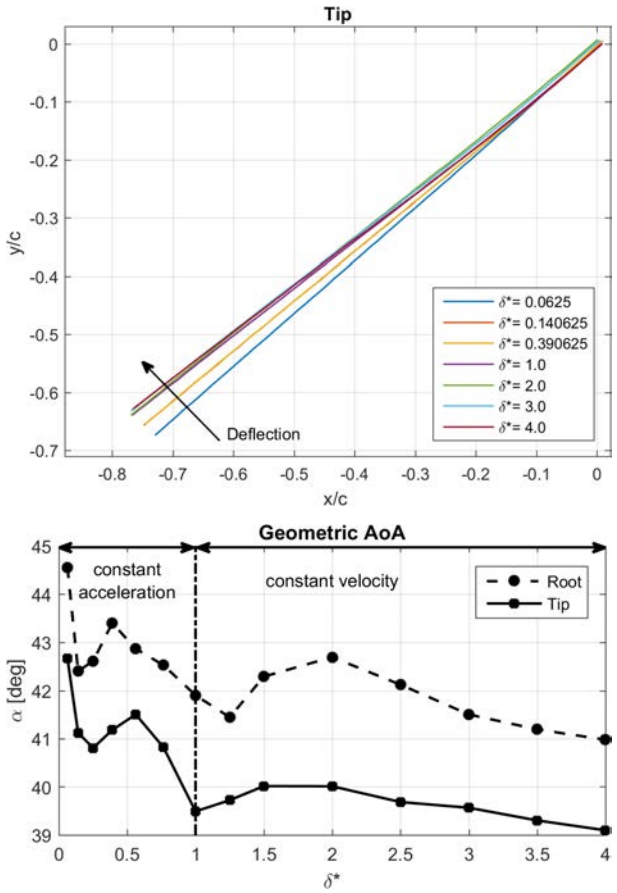

175 [μm] Moderate flexibility

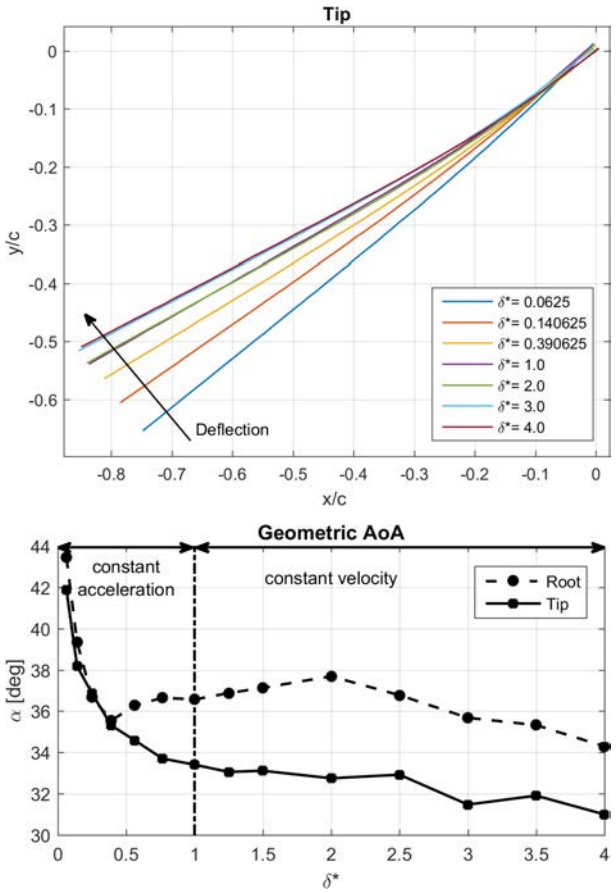

125 [μm] High flexibility

Fig. 5 Chord profile deflection at the tip (*Top*) and temporal evolution of geometric angle of attack (*Bottom*). *Left:* 175 [μm] moderate flexible wing. *Right:* 125 [μm] high flexible wing.

The chordwise variation of the local angle of attack at the tip and the spanwise distribution of the geometric angle of attack at $\delta^* = 4$ are given in Fig. 6 for the high flexibility wing.

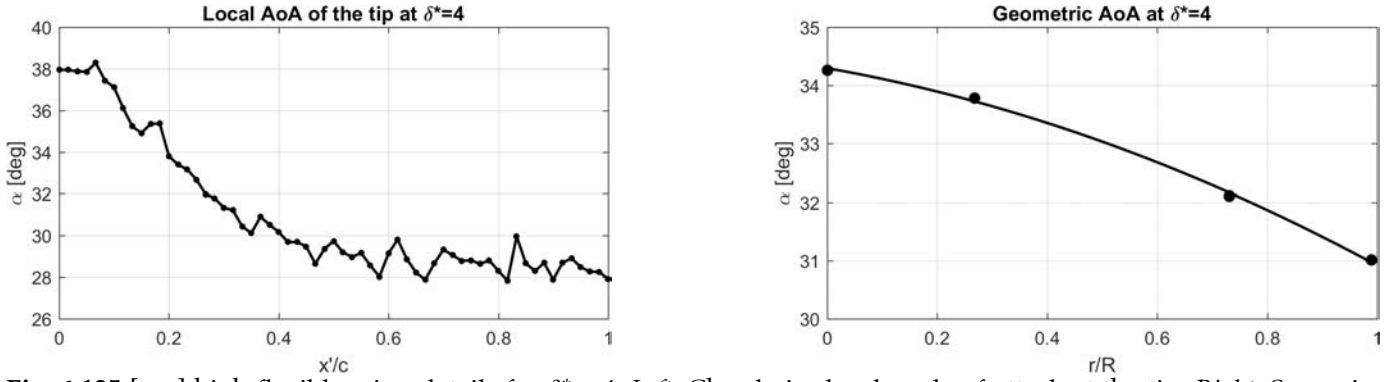

Fig. 6 125 [μm] high flexible wing details for $\delta^* = 4$. *Left:* Chordwise local angle of attack at the tip. *Right:* Spanwise distribution of the geometric angle of attack.

As can be deduced from the shape of the flexible wings during the revolving motion (see Fig. 5), the maximum deformation occurs close to the leading edge resulting in a prominent variation of the local angle of attack for the chordwise locations from the leading edge ($x/c = 0$) until approximately $x/c = 0.4$, after which it is mostly constant (see Fig. 6 *left*). Furthermore, it can be observed that the geometric angle of attack changes approximately linearly over the span indicating the formation of wing twist.

Force measurements

In Fig. 7, the temporal evolution of the lift and drag characteristics for the different wings considered in this study (i.e., rigid, moderate flexibility and high flexibility) are given.

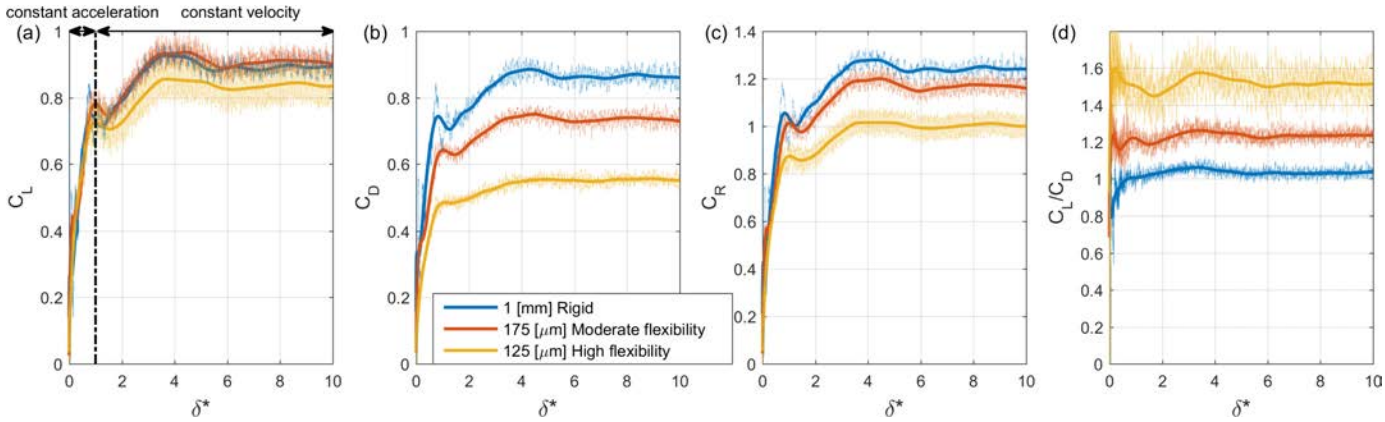

Fig. 7 Temporal evolution of (a) lift, (b) drag, (c) resultant force ($\boldsymbol{C_R = \sqrt{C_L^2 + C_D^2}}$) and (d) lift-to-drag ratio characteristics for different flexibilities. The light background signal is the ensemble average of the raw lift and drag data, and the thick solid line is the corresponding low-pass-filtered data.

The drag and lift for the rigid wing are comparable, with the angle of attack being 45 deg, which confirms that the pressure forces are dominant, so that the net force vector is oriented normal to the wing surface. For all wing cases, the forces build up rapidly at the start of the motion due to non-circulatory added mass effects. The added mass reaction force acts normal to the local wing surface and is proportional to the acceleration component in this direction. Therefore, for the rigid wing, its contribution is constant throughout the acceleration phase. However, for the flexible wings, the acceleration component in the wing-normal direction changes since the wings deform (see Fig. 5) and so does the magnitude of the added mass force. In addition to the added mass reaction force, circulatory forces associated with the generation of the LEV build up gradually with increasing velocity. At the end of the acceleration phase, there is a slight decrease in the force coefficients as the added mass contribution ceases to contribute. After the acceleration phase, the lift and drag continue to increase until a maximum is reached at approximately $\delta^* = 4.5$. Subsequently, the forces decrease slightly until for all wings nearly steady-state conditions are reached at approximately $\delta^* = 5$.

The comparison of the lift data shows that the lift generation of the rigid and the moderate flexible wings are comparable, while smaller lift levels are achieved in the high flexibility case. The drag shows a monotonic decrease with decreasing flexural stiffness. At steady-state conditions, for $\delta^* = 10$, the lift coefficients of the high flexible wing is approximately 7% lower compared to the rigid wing, while the lift coefficient of the moderate flexible wing is approximately 1% higher. The steady-state drag coefficients of the moderate and high flexible wings are respectively 15% and 36% lower compared to the rigid wing, which results in an approximate increased lift-to-drag ratio of respectively 18% and 45% . The resultant force acting on the model is decreased with decreasing flexural stiffness throughout the revolving motion. For steady-state conditions the resultant force coefficient of the moderate and high flexibility are respectively 6% and 19% lower compared to the rigid wing.

At the leading edge of the wing the flow separates and a LEV is formed which is accompanied by the formation of a low pressure region. The associated suction forces acting normal to the wing surface are the dominant factor determining the net forces acting on the wing. As a result the net force vector for a rigid wing acts normal to the wing surface, such that (Usherwood & Ellington, 2002),

$$\alpha_{geo} = \tan^{-1}(D/L) \qquad (7)$$

However, flexible wings deflect which leads to a deviation of the net force vector orientation with respect to the angle of attack that is initially set at the leading edge (Zhao et al., 2009). Based on Equation 7 the geometric angles of attack α_{geo} at $\delta^* = 4$ for the rigid, moderate flexible and high flexible wings are calculated to be 43.7 deg, 38.6 deg and 32.6 deg, respectively. A comparison with the wing reconstruction results is given in Table 2.

Tab. 2 Comparison of the geometric angle of attack α_{geo} based on the wing reconstruction (Fig. 5) and the lift-to-drag ratio (Equation 7). Results apply to $\delta^* = 4$.

Wing	α_{geo} root [deg] Wing reconstruction (Fig. 5)	α_{geo} tip [deg] Wing reconstruction (Fig. 5)	α_{geo} [deg] Force relation (Equation 7)
1 [mm] Rigid	45	45	43.7
175 [μm] Moderate flexibility	41	39	38.6
125 [μm] High flexibility	34.5	31	32.6

Although the presented wing reconstruction in this section is an approximation of the true wing shape, it can be observed that the reconstructed geometric angles of attack near the tip of the wing agree well with the direction of the net force for the studied wings. This observation suggests that for a chordwise flexible wing the lift-to-drag ratio at steady-state conditions can be estimated based on the geometric angle of attack as illustrated in Fig. 8.

Fig. 8 Net force angle as a function of geometric angle of attack *Left:* Rigid wing. *Right:* Flexible wing. Apparent reference flow from left-to-right. Small vectors represent local net forces that act normal to the wing surface, and big vector represent resultant net force that is aligned with respect to the geometric angle of attack.

Vortical Structures

The vortical structures are identified using the Q-criterion, $Q = -\frac{1}{2}\frac{\partial u_i}{\partial u_j}\frac{\partial u_j}{\partial u_i}$, (Hunt et al., 1988) which represents the local balance between shear strain rate and vorticity magnitude, such that a positive value of the Q-criterion indicates regions that are dominated by rotation. Although the Q-criterion is not rotation invariant, i.e. the components du_x/dz (spanwise variation of chordwise velocity) and du_z/dx (chordwise variation of spanwise velocity) are different in the rotating reference frame compared to the inertial reference frame when revolving around the y-axis, the identified Q-criterion isosurfaces are very similar and the differences are negligible. The vortical structures are colored by helical density $h = \boldsymbol{u}\cdot\boldsymbol{\omega}$, $\boldsymbol{u}$ being the velocity vector and $\boldsymbol{\omega}$ being the

vorticity vector (Moffatt, 1969), which is indicative for the vorticity flux along the primary axis of a vortex. The helical density is calculated in the inertial reference frame such that the vorticity flux along the primary axis of a vortex is indicative for the spanwise and chordwise advection of vorticity.

In Fig. 9 the vortical structures that are colored by helical density are depicted for the three wings at $\delta^* = 1$ and $\delta^* = 1.5$. The global topology of the vortex system for the three wing models is similar, although the orientation of the structures is clearly affected by the wing deformation. For each wing a LEV, an initial coherent starting TEV with a number of smaller scale TEVs, a TV and a root vortex (RV) are present. The vortex system for the flexible wings is more coherent with the most significant difference occurring for the RV. From the side views the greater tip deflection for the flexible wings compared to the rigid wing can be observed.
For $\delta^* = 1$ it can be observed that in relation to the chordwise deflection of the wings, the TV and the starting vortex system is more elongated in the streamwise direction in the flexible cases. As a result, the vortical structures in the wake are confined to a significantly smaller region. For decreasing flexural stiffness, the finger-like swirling vortices that are wrapped circumferentially around the TV are located closer to the center of the TV. These finger-like vortices can be seen to connect to the secondary small-scale TEVs in all cases. At $\delta^* = 1.5$, a large number of secondary TEVs are present elongating all over the span in the wake. The flexible wings appear to shed a higher ordered and more continues streak of smaller-scale TEVs compared to the rigid wing. The TEVs move downstream along approximately the local induced angle of attack at the trailing edge of the wing model. Near midspan ($r/R = 0.5$), the core of the LEV is expanded into a substantial bubble-like structure that extends towards to the tip for all three wings. The LEV grows in size along the span until about 75% of the span length. For $\delta^* > 1.5$ there is an onset of vortex burst at which the vortex formation starts displaying significant small scale chaotic structures, which appears quite similar for all wings.

The highest positive and negative helical density levels exist in the LEV and TV, respectively. However, the high positive levels are more coherent with decreasing flexural stiffness. These high levels of helical density are indicative of an outboard spanwise vorticity flux along the axis of the LEV which is associated with the spanwise transport of vorticity contributing to the stability of the LEV.

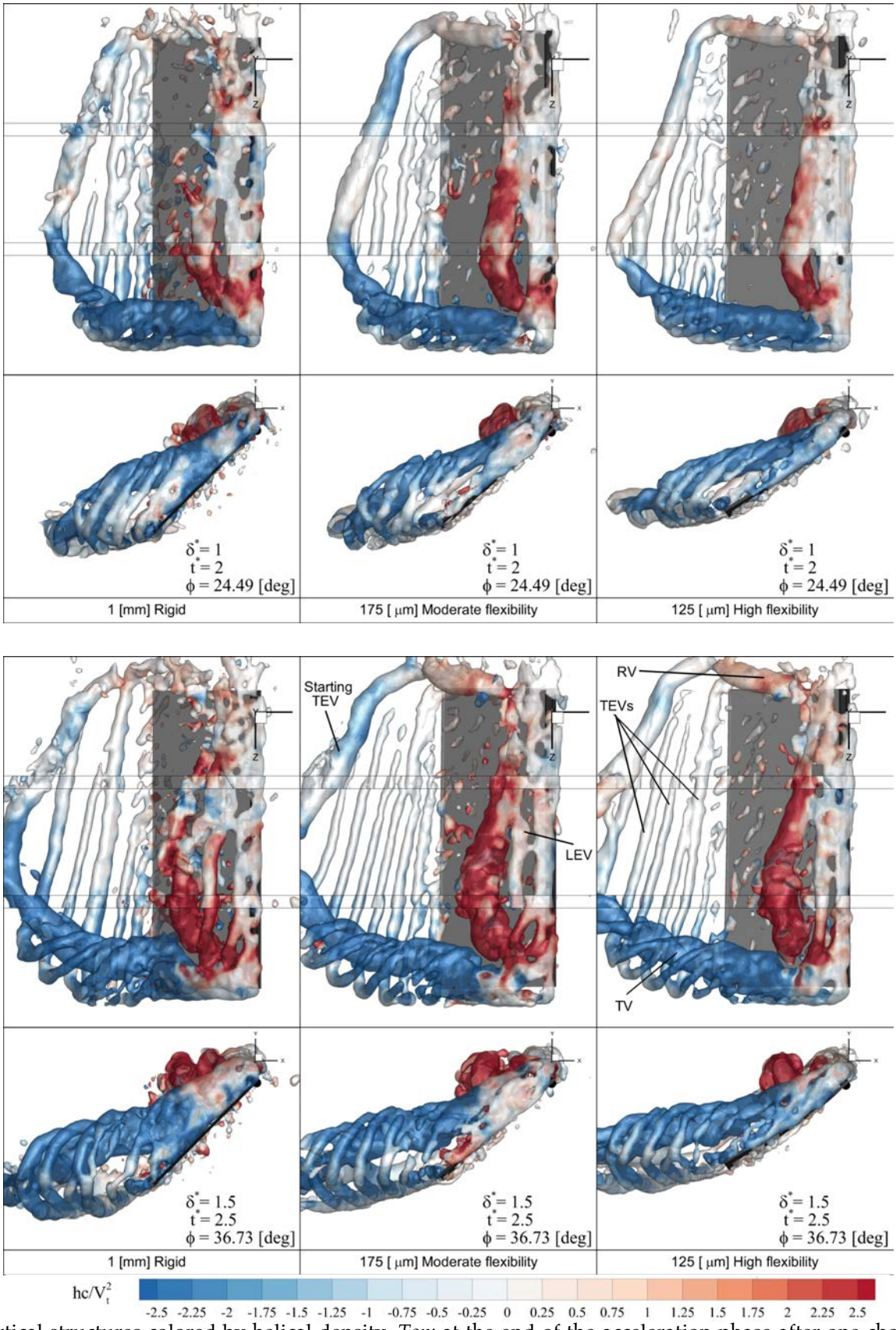

Fig. 9 Vortical structures colored by helical density. *Top:* at the end of the acceleration phase after one chord length of travel ($\delta^* = 1$), *Bottom:* after $\delta^* = 1.5$. White isosurfaces of Q-criterion ($Q/(V/c)^2 = 3$) colored by helical density (hc/V^2). The vortex system consists of a starting trailing edge vortex (starting TEV), multiple shed trailing edge vortices (TEVs), a tip vortex (TV), a root vortex (RV) and a leading edge vortex (LEV).

Pressure field

In Fig. 10, the pressure contours are given in chordwise oriented planes along the span, and at 50% and 75% span locations for $\delta^* = 1.5$ and 4. The low pressure region at the suction side of the wing correlates well with the location of the LEV, as depicted in Fig. 9. At $\delta^* = 1.5$, a low pressure region is observed downstream of the wing which is associated with the starting TEV. At midspan ($r/R = 0.5$), the location of the low pressure region is similar for the different wings. At $\delta^* = 4$ the low pressure region accompanied by the LEV reduces in size for decreasing flexural stiffness. Also the high pressure region on the lower side of the wing becomes slightly smaller in size, such that the net pressure difference between the pressure and suction side of the airfoil is significantly decreased with decreasing flexural stiffness, which correlates well with the reduction in the resultant force acting on the wing observed in the balance measurements (see Fig. 7). Although the low pressure region associated with the LEV is reduced in size with decreasing flexural stiffness, resulting in a smaller resultant force on the wing, the corresponding lift generation remains relatively high because of the increased alignment of the force vector in the direction of the lift caused by the wing deformation and the relative high suction peak that is located closer to the wing surface. These observations suggesting a reduction of the total net force and an increase of the lift-to-drag ratio agree well with the balance measurements, as depicted in Fig. 7.

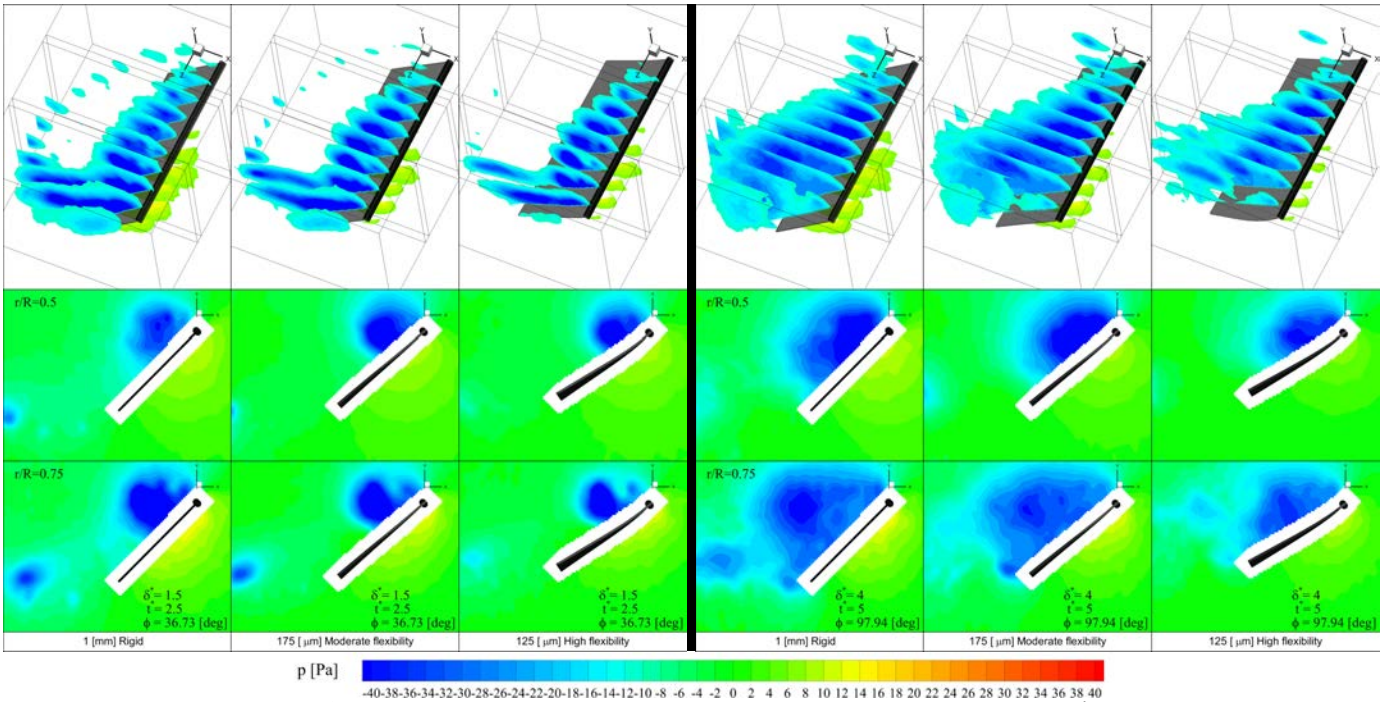

Fig. 10 Pressure contours (p). *Left:* $\delta^* = 1.5$ and *Right:* $\delta^* = 4$. Top: Pressure contours along the span. *Middle:* Pressure contour at $r/R = 0.5$. *Bottom:* Pressure contour at $r/R = 0.75$.

In Fig. 11 the footprint of the wake, as identified by a low pressure region, is given in a spanwise oriented plane located at 0.5*c* distance downstream from the trailing edge. Due to the deflection of a flexible wing, the flow becomes more aligned with the freestream flow at the trailing edge and a smaller wake is formed which is especially pronounced in the vicinity of the shed tip vortex. The reduced size and magnitude of the low pressure region in the wake associated with the deflection of the wing, which also results in tilting of the reduced net resultant force vector in the lift direction, accounts for the significant decrease in drag with increasing wing flexibility.

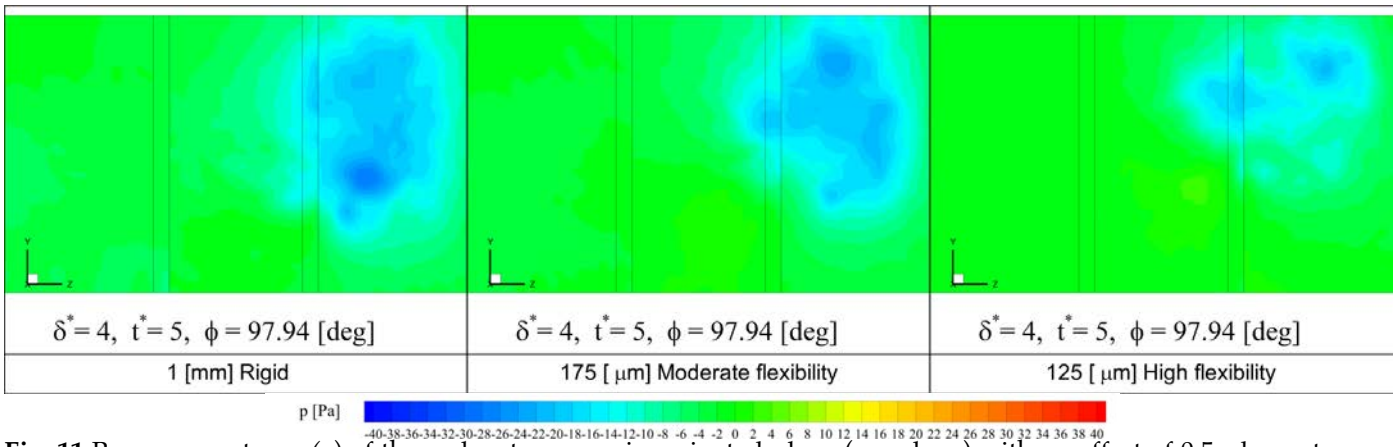

Fig. 11 Pressure contours (*p*) of the wake at a spanwise oriented plane (y,*z*-plane) with an offset of 0.5*c* downstream of the trailing edge for $\delta^* = 4$.

In Fig. 12 the low (blue) and high (red) pressure regions are given in conjunction with the vortical structures for $\delta^* = 1.5$ and 4. The vortical structures are dominated by rotation in which a low pressure region is created. It can be observed that the transition of the pressure field between the volumes is relatively smooth and that the low pressure regions correlate well with the vortical structures. Consequently, it can be observed that the vortical structures overlap with the calculated low pressure regions. Regions of decreased pressure corresponding to the small-scale vortical features are not resolved due to the limited spatial resolution and smoothing nature of the Poisson pressure integration scheme. As mentioned earlier the size of the low pressure region is decreasing with decreasing flexural stiffness, which can be observed by the smaller blue isosurface regions for decreasing flexural stiffness. The high pressure region (red) is mainly located outboard of midspan ($r/R > 0.5$) and also decreases in size with decreasing flexural stiffness.

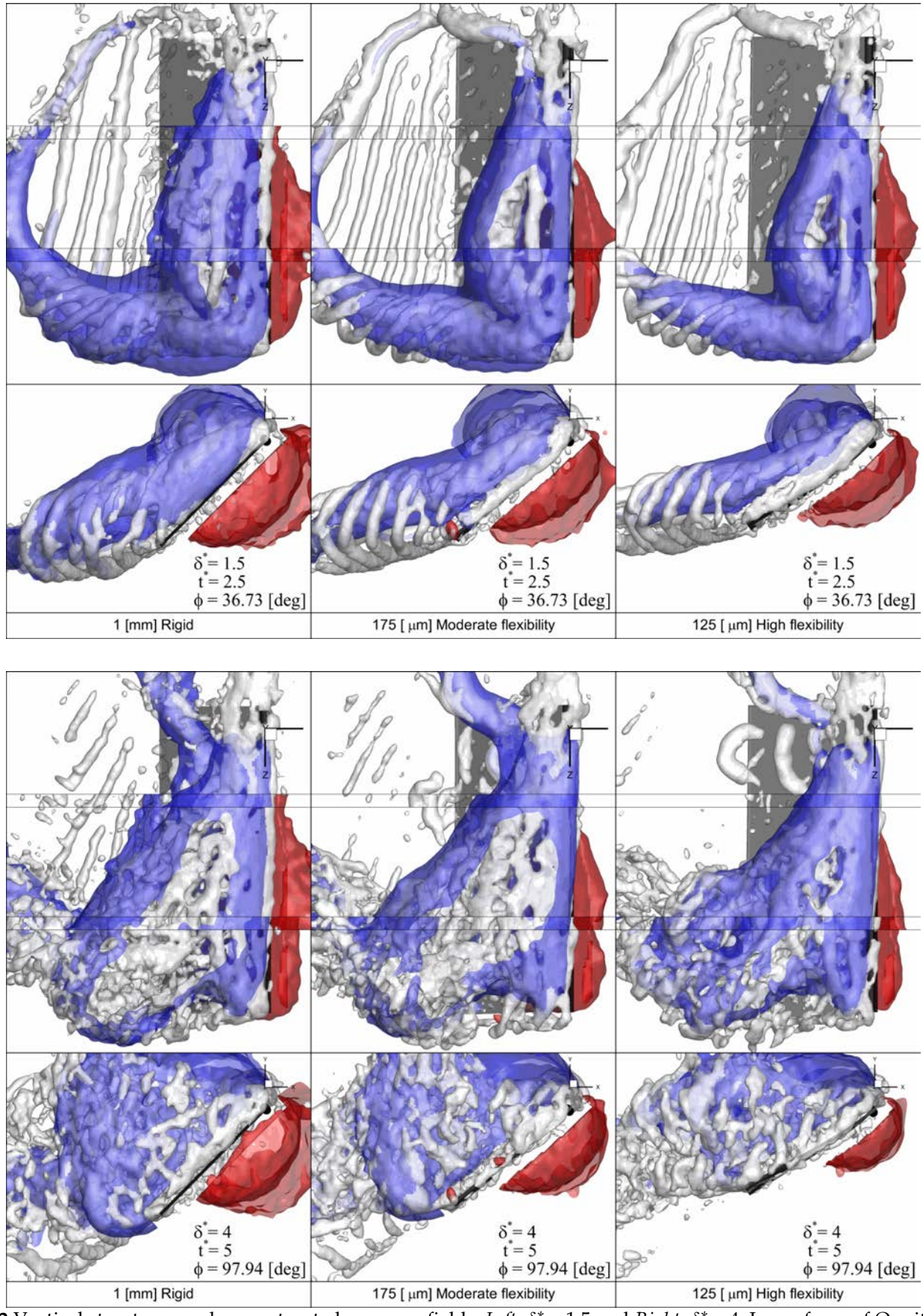

Fig. 12 Vortical structures and reconstructed pressure fields. *Left:* $\delta^* = 1.5$ and *Right:* $\delta^* = 4$. Isosurfaces of Q-criterion: White ($Q/(V_i/c)^2 = 3$). Isosurfaces of reconstructed pressure field: Blue p = -13 Pa and Red p = 6 Pa.

Since the pressure field is independent of the reference frame and the Q-criterion is similar in both rotating and inertial reference frame for the current flow case, it is expected that the pressure field is directly related to the Q-criterion because the latter is essentially the source term of the Poisson pressure integration scheme for an incompressible flow in the absence of rotational effects. Although $Q > 0$ does not guarantee the existence of a pressure minimum, in most cases they are equivalent (Jeong, 1995). In this study also a high correlation between the low pressure field and Q-criterion is observed.

Spanwise distribution of LEV circulation, LEV centroid, LEV pressure centroid, and sectional lift and drag coefficients for δ^*= 1, 1.5 and 4.

In Fig. 13 the LEV circulation, the LEV centroid, the LEV pressure centroid and the sectional lift and drag coefficients for $\delta^* = 1$, 1.5 and 4 are given. The LEV circulation is calculated based on the spanwise component of vorticity as,

$$\Gamma^*_{LEV} = \int_{S_{xy}} \frac{\omega_z}{cV_t} dxdy \quad (8)$$

and the LEV centroid in x,y-coordinates is calculated as,

$$LEV\ Cen._{\boldsymbol{x}} = \frac{\int_{S_{xy}} \boldsymbol{x}\omega_z dxdy}{\int_{S_{xy}} \omega_z dxdy} \quad (9)$$

where **x** is the x,y-coordinate at a chordwise orientated plane and S_{xy} is the chordwise integration region for which $\gamma_2 > 2/\pi$ as described by Graftieaux et al. (2001). The LEV pressure centroid is calculated analogous to the LEV centroid using the pressure information in Equation. 9 instead of the spanwise vorticity information. From the LEV (pressure) centroid x,y-coordinates and the wing reconstruction information, the distance of the LEV (pressure) centroid to the wing surface is calculated. The lift and drag coefficients are calculated according to the procedure outlined in Section 3, Equations 5 and 6.

Until the end of the acceleration period ($\delta^* = 1$) all wings display very similar characteristics in terms of the LEV properties and sectional force coefficients. Subsequently, at about $\delta^* > 1.5$ a transition period appears to occur which correlates with the onset of vortex breakdown. Finally, at approximately $\delta^* = 4$, the spanwise distribution is settled and approximate steady-state conditions are reached. The LEV circulation at $\delta^* = 1$ is similar for the different wings and shows

a linear increase in the spanwise direction until $r/R = 0.9$ which is associated with the increase of the rotational velocity due to the curvilinear nature of the motion, after which it decreases to zero at the tip. At steady-state conditions ($\delta^* = 4$), the circulation inboard of midspan ($r/R < 0.5$) is similar for the different wings, while outboard of midspan the circulation decreases significantly with decreasing flexural stiffness.

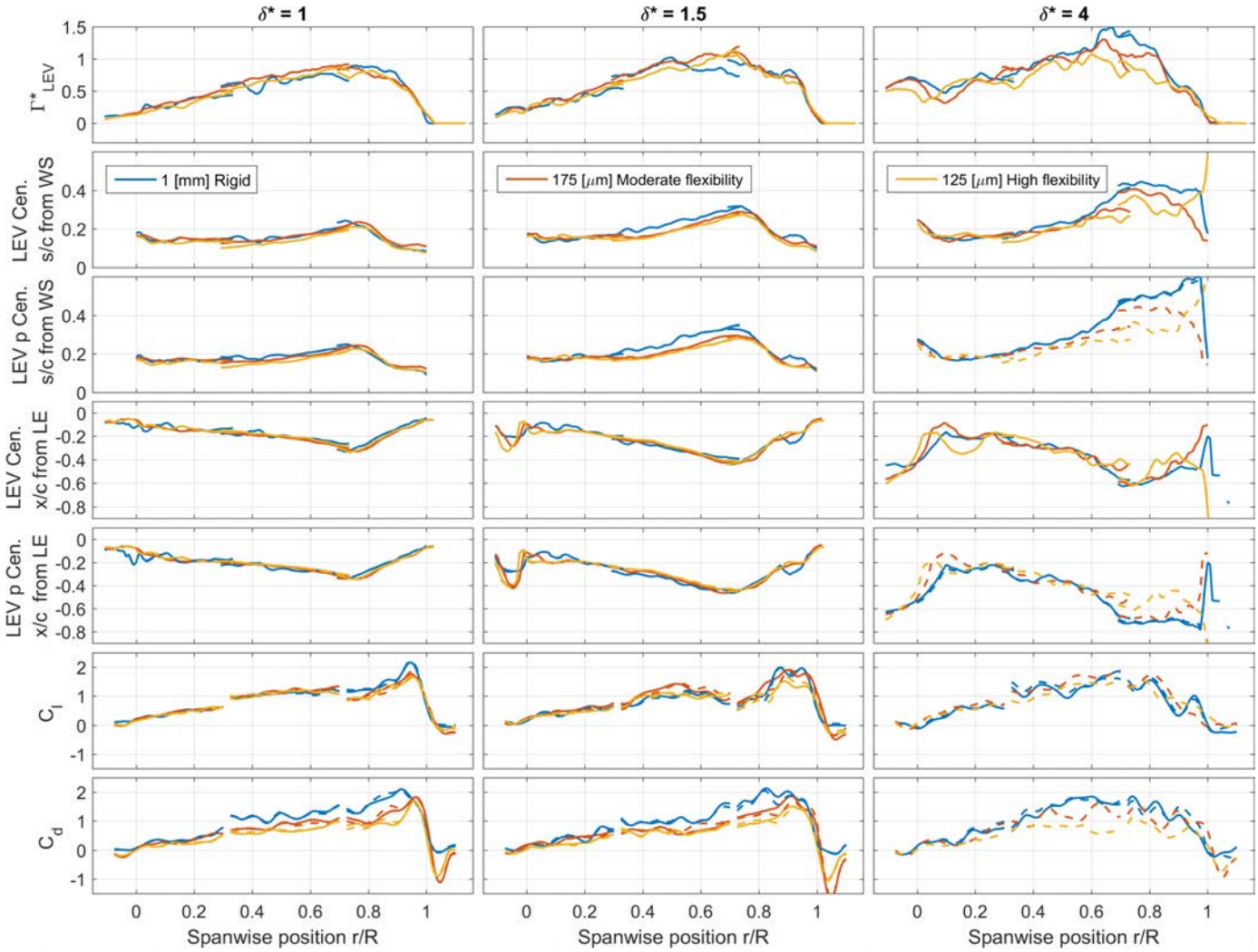

Fig. 13 Spanwise characteristics for $\delta^* = 1$, 1.5 and 4. From the top to bottom row respectively: LEV circulation (Γ^*_{LEV}), LEV centroid chord distance (s/c) normal to wing surface (WS), LEV pressure centroid chord distance (s/c) normal to wing surface (WS), LEV centroid chord distance in the x-direction (x/c) from leading edge (LE), LEV pressure centroid chord distance in the x-direction (x/c) from leading edge (LE), Sectional lift coefficient (C_l) and Sectional drag coefficient (C_d) as a function of spanwise position along the span (r) non-dimensionalized with the span length (R). The sectional control volumes have a spanwise thickness of $dz = 7$ vectors and an overlap of 6 vectors. For the LEV pressure centroid and the sectional lift & drag, the solid line depicts a temporal resolution of TR* = 0.25 and the dashed line depicts a coarsened temporal resolution of TR* = 0.5.

The LEV centroid and the LEV pressure centroid have a high correlation for the different flexibilities with the most pronounced difference near the tip at $\delta^* = 4$. This agreement between LEV and pressure centroid positions is in accordance with Fig. 12 in which the LEV structure

correlates well with the low pressure region. It can be observed that the LEV pressure centroid is located significantly closer to the wing surface for decreasing flexural stiffness. This is most pronounced outboard of midspan ($r/R > 0.5$) at $\delta^* = 4$ and correlates with the observations of the spanwise pressure fields, as depicted in Fig. 10. The aft tilt of the LEV is approximately similar for the different flexibilities, except near the tip ($r/R > 0.6$) at $\delta^* = 4$, which corresponds with the bubble-like structure, at which the LEV is tilted less aft with decreasing flexural stiffness. The sectional lift and drag at the end of the acceleration ($\delta^* = 1$) show a linear increase with spanwise position until approximately $r/R = 0.9$ which correlates with the increase in rotational velocity and LEV circulation. The spanwise oscillations in the sectional lift and drag mainly originate from the momentum flux contribution in the calculations based on the control volume approach. While the sectional lift for the different wings is comparable, a significant decrease in sectional drag can be observed with decreasing flexural stiffness. These observations are in accordance with the behavior of the total forces as determined by the balance measurements (see Fig. 7). While the sectional drag inboard of $r/R = 0.3$ is approximately similar for the different wings, the sectional drag considerably decreases with the flexural stiffness at the outboard locations. The spanwise centroids of the lift and drag are located at approximately 70% of the span for all the cases throughout the complete motion.

5. Conclusion

The flow fields and fluid-dynamic loads generated by revolving low-aspect-ratio flat-plate wings with different degree of chordwise flexibility are experimentally studied using tomographic PIV and simultaneous force measurements. Three different wings were tested in the experiments in order to investigate the influence of wing flexibility: a rigid wing from 1 mm thick Plexiglass, a moderately flexible wing from 175 μm PET and a highly flexible wing from 125 μm PET.

The force measurements reveal that during the acceleration phase the build-up of lift is similar for the different wings, while the build-up of drag is significantly lower for decreasing flexural stiffness. At steady-state conditions the net resultant force generation is decreased significantly with decreasing flexural stiffness. However, this does is not adversely affect the lift generation such that the lift coefficients for the rigid and the moderate wings are very similar, while it is only slightly (about 7%) smaller for the high flexible wing. On the other hand, the drag decreases monotonically with decreasing flexural stiffness, up to 36% for the most flexible wing, which corresponds to an increased lift-to-drag ratio of approximately 45%. It is further found that for

the wings models considered in this study the lift-to-drag ratio at the steady-state conditions for the chordwise flexible wings correlates well with the geometric angle of attack of the deformed structure near the wing tip.

A similar vortex system, comprising LEV, TV, RV and starting TEV components, are observed in all cases. For decreasing flexural stiffness, the coherency of this vortex system is increased. Furthermore, the LEV structure of the flexible wings shows higher helical density values compared to the rigid wing and are indicative for an outboard spanwise vorticity flux along the axis of the LEV which is associated with the spanwise transport of vorticity contributing to the stability and retention of the LEV.

At low Reynolds numbers the flow field is highly repeatable, notably for the initial development phase of the flow considered in the present experiments, which allows obtaining temporal information from phase-locked measurements. The pressure field and loads have been reconstructed successfully from ensemble averaged phase-locked tomographic PIV measurements for different flexible wings, employing the non-inertial moving reference frame of the rotating wing. Furthermore, the pressure field that covers a complete wing has been successfully reconstructed from three volumes that have been measured independently, which allowed a proper comparison of pressure fields between different wings. The vortex system structures encompass a low pressure region which has a high correlation with the vortical structures identified by the Q-criterion. As a result a comparative assessment between the different wings regarding the size of the low pressure zone associated to the LEV as well as the size of the wake can be made on the basis of the Q-criterion.

Due to the same predefined local angle of attack of 45 deg at the leading edge for the different wings, the circulation of the flexible wings is relatively high and over a large extent of the span and revolving motion similar to that of the rigid wing. The location of the LEV pressure centroid correlates well with the LEV centroid. Consequently, the LEV center of pressure can be approximated with the LEV center. The LEV pressure centroid location is similar for the different wings in absolute sense. However, due to the deflection of the flexible wings, the LEV pressure centroid is located closer to the wing surface. As the low pressure region accompanying the LEV becomes smaller with increasing flexibility, the total force acting on the wing is reduced, but it is also tilted more towards the lift direction due to the wing deformation. As a consequence, the lift component remains relatively high, also because the suction peak is located closer to the wing

surface. Simultaneously, the drag is significantly suppressed for increasing flexibility, which is also reflected in the smaller size of the wake. While the sectional lift along the full span is comparable for the different wings, the sectional drag is significantly reduced at the outboard wing locations for increasing flexibility.

References

Anderson J, (2011) Fundamentals of Aerodynamics. McGraw-Hill, New York

Beals N, Jones AR (2015) Lift Production by a Passively Flexible Rotating Wing. AIAA Journal 53(10): 2995–3005

Birch JM (2004) Force production and flow structure of the leading edge vortex on flapping wings at high and low Reynolds numbers. Journal of Experimental Biology 207(7):1063–1072.

Carr ZR, Chen C, Ringuette MJ (2013) Finite-span rotating wings: three-dimensional vortex formation and variations with aspect ratio. Experiments in Fluids 54(2):1444.

Combes SA, TL Daniel (2003) Flexural stiffness in insect wings I. Scaling and the influence of wing venation. Journal of Experimental Biology 206(17):2979–2987.

de Kat R, van Oudheusden BW (2012) Instantaneous planar pressure determination from PIV in turbulent flow. Experiments in Fluids 52(5):1089–1106.

Ellington CP, van den Berg C, Willmott AP, Thomas ALR (1996) Leading-edge vortices in insect flight. Nature 384(6610):626–630.

Elsinga GE, Scarano F, Wieneke B, van Oudheusden BW (2006) Tomographic particle image velocimetry. Experiments in Fluids 41(6):933–947.

Graftieaux L, Michard M, Grosjean N (2001) Combining PIV, POD and vortex identification algorithms for the study of unsteady turbulent swirling flows. Measurement Science and Technology 12(9):1422–1429.

Hunt JCR, Wray AA, Moin P (1988) Eddies, stream, and convergence zones in turbulent flows. Center for Turbulence Research Report CTR-S88:193-208.

Jardin T, David L (2014) Spanwise gradients in flow speed help stabilize leading-edge vortices on revolving wings. Physical Review E 90(1):013011.

Jardin T, David L (2015) Coriolis effects enhance lift on revolving wings. Physical Review E 91(3):031001.

Jeong J, Hussain F (1995) On the identification of a vortex. Journal of Fluid Mechanics 285:69-94.

Jones AR, Babinsky H (2010) Unsteady Lift Generation on Rotating Wings at Low Reynolds Numbers. Journal of Aircraft 47(3):1013–1021.

Lentink D, Dickinson MH (2009) Rotational accelerations stabilize leading edge vortices on revolving fly wings. Journal of Experimental Biology 212(16):2705–2719.

Moffatt HK (1969) The degree of knottedness of tangled vortex lines. Journal of Fluid Mechanics 35(1):117-129.

Ozen CA, Rockwell D (2012) Flow structure on a rotating plate. Experiments in Fluids 52(1):207–223.

Percin M, van Oudheusden BW (2015a) Flow Visualization and Force Measurements on Accelerated Revolving Flat Plates at Low Reynolds Numbers. In 45th AIAA Fluid Dynamics Conference (pp. 1–12). doi:10.2514/6.2015-3074

Percin, M, & van Oudheusden BW (2015b) Three dimensional flow structures and unsteady forces on pitching and surging revolving flat plates. Experiments in Fluids 56(2):1–19

Poelma C, Dickson WB, Dickinson MH (2006) Time-resolved reconstruction of the full velocity field around a dynamically-scaled flapping wing. Experiments in Fluids 41(2):213–225.

Sane SP (2003) The aerodynamics of insect flight. Journal of Experimental Biology 206(23):4191–4208.

Scarano F (2013) Tomographic PIV: principles and practice. Measurement Science and Technology 24(1):012001.

Shyy W, Aono H, Chimakurthi SK, Trizila P, Kang CK, Cesnik CES, Liu H (2010) Recent progress in flapping wing aerodynamics and aeroelasticity. Progress in Aerospace Sciences 46(7):284–327.

Tronchin T, David L, Farcy A (2015) Loads and pressure evaluation of the flow around a flapping wing from instantaneous 3D velocity measurements. Experiments in Fluids 56(1):7.

Usherwood JR, Ellington CP (2002) The aerodynamics of revolving wings I. Model hawkmoth wings. The Journal of Experimental Biology 205(11):1547–64.

van Oudheusden BW (2013). PIV-based pressure measurement. Measurement Science and Technology 24(3):032001.

Vanyo J (2015) Rotating Fluids in Engineering and Science. Elsevier Science, Stoneham

Wolfinger M, Rockwell D (2014) Flow structure on a rotating wing: effect of radius of gyration. Journal of Fluid Mechanics 755(8):83–110.

Zhao L, Huang Q, Deng X, Sane SP (2009) Aerodynamic effects of flexibility in flapping wings. Journal of The Royal Society Interface 7(44):485–497.

Zhao L, Deng X, Sane SP (2011). Modulation of leading edge vorticity and aerodynamic forces in flexible flapping wings. Bioinspiration & Biomimetics 6(3):036007.